



OPEN

Sequential delithiation behavior and structural rearrangement of a nanoscale composite-structured $\text{Li}_{1.2}\text{Ni}_{0.2}\text{Mn}_{0.6}\text{O}_2$ during charge–discharge cycles

Keiji Shimoda¹✉, Koji Yazawa², Toshiyuki Matsunaga¹, Miwa Murakami¹, Keisuke Yamanaka³, Toshiaki Ohta³, Eiichiro Matsubara⁴, Zempachi Ogumi¹ & Takeshi Abe⁵

Lithium- and manganese-rich layered oxides (LMRs) are promising positive electrode materials for next-generation rechargeable lithium-ion batteries. Herein, the structural evolution of $\text{Li}_{1.2}\text{Ni}_{0.2}\text{Mn}_{0.6}\text{O}_2$ during the initial charge–discharge cycle was examined using synchrotron-radiation X-ray diffraction, X-ray absorption spectroscopy, and nuclear magnetic resonance spectroscopy to elucidate the unique delithiation behavior. The pristine material contained a composite layered structure composed of Ni-free and Ni-doped Li_2MnO_3 and LiMO_2 ($M = \text{Ni}, \text{Mn}$) nanoscale domains, and Li ions were sequentially and inhomogeneously extracted from the composite structure. Delithiation from the LiMO_2 domain was observed in the potential slope region associated with the $\text{Ni}^{2+}/\text{Ni}^{4+}$ redox couple. Li ions were then extracted from the Li_2MnO_3 domain during the potential plateau and remained mostly in the Ni-doped Li_2MnO_3 domain at 4.8V. In addition, structural transformation into a spinel-like phase was partly observed, which is associated with oxygen loss and cation migration within the Li_2MnO_3 domain. During Li intercalation, cation remigration and mixing resulted in a domainless layered structure with a chemical composition similar to that of $\text{LiNi}_{0.25}\text{Mn}_{0.75}\text{O}_2$. After the structural activation, the Li ions were reversibly extracted from the newly formed domainless structure.

The world is moving towards electrification as CO_2 emission standards have resulted in a growing battery market. Rechargeable lithium ion batteries (LIBs) have been widely used as a power source for portable devices and currently the global market for electric vehicles (EVs) demands higher power, higher energy density, longer life, and lower cost batteries. A significant amount of effort has been dedicated to the development of improved battery materials, with recent studies investigating lithium- and manganese-rich layered oxides (LMRs), which are preferred candidate materials for the next-generation LIB positive electrodes due to their high reversible capacities of $\geq 200 \text{ mA h g}^{-1}$ at 2.0–4.8 V^{1–10}. In contrast, several drawbacks have been reported including capacity fading and voltage decay during long-term charge–discharge cycles^{6–14}. The structural factors resulting in these problems must be solved to develop stable and high power batteries.

LMRs exhibit a layered rock-salt structure commonly represented as $\text{Li}[\text{Li}_{(1-2x)/3}\text{M}_x\text{Mn}_{(2-x)/3}]\text{O}_2$ ($M = \text{Ni}, \text{Co}$, etc.) in single-phase notation or as $x\text{Li}_2\text{MnO}_3 \cdot (1-x)\text{LiMO}_2$ in composite notation. Based on single-phase notation, the crystal structure can be indexed with a space group of $C2/m$, where the structure is homogeneous and Li ions occupy the Li layer and part of the transition-metal (TM) layer with intralayer ordering between the Li and TM ions. In contrast, the composite notation can be expressed as a mixture of $C2/m$ and $R\bar{3}m$ structures, where Li_2MnO_3 (alternatively expressed as $\text{Li}[\text{Li}_{1/3}\text{Mn}_{2/3}]\text{O}_2$) and LiMO_2 exhibit common d spacing. These two phases are dispersed as nanoscale domains over the entire structure¹⁵. Unfortunately, X-ray diffraction (XRD)

¹Office of Society-Academia Collaboration for Innovation, Kyoto University, Uji, Kyoto, 611-0011, Japan. ²JEOL RESONANCE Inc., Akishima, Tokyo, 196-8558, Japan. ³SR Center, Ritsumeikan University, Kusatsu, Shiga, 525-8577, Japan. ⁴Department of Materials Science and Engineering, Kyoto University, Kyoto, 606-8501, Japan. ⁵Gradual School of Global Environmental Studies, Kyoto University, Katsura, Nishikyō, Kyoto, 615-8510, Japan. ✉e-mail: shimoda.keiji.6v@kyoto-u.ac.jp

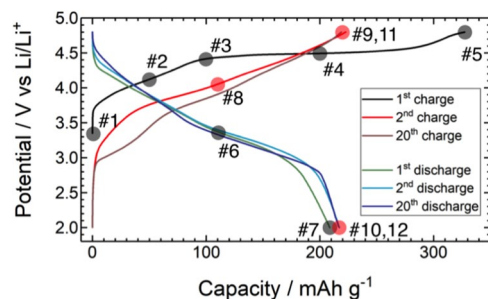


Figure 1. Charge–discharge profiles of the Li//Li_{1.2}Ni_{0.2}Mn_{0.6}O₂ cell at the 1st, 2nd, and 20th cycles. The electrochemical measurements were performed at 50 °C between 2.0 and 4.8 V vs. Li/Li⁺ at a constant current of 20.5 mA g⁻¹. The sampling points are marked.

studies provided no clear indication of which structural model appropriately represents the real structure. Many atomic column observations using advanced scanning transmission electron microscopy (STEM) have provided evidence of two structural domains in the composite structure^{16–19}, while other reports showed a homogeneous atomic column, suggesting a single-phase structure^{20–22}. Solid-state nuclear magnetic resonance (NMR) spectroscopy is sensitive to cation substitution in the first and second cation coordination shells, allowing the local structure to be examined at a length scale of <5 Å in diameter. Grey *et al.* reported the nonrandom cation distribution around Li ions in Li[Li_{(1–2x)/3}M_xMn_{(2–x)/3}]O₂ via ⁶Li magic-angle spinning (MAS) NMR analyses, implying a composite nature instead of homogeneous solid solution^{23–25}.

Lithium deintercalation causes continuous changes of the *a* and *c* lattice parameters of LMRs^{26–29}. These changes are closely associated with the charge compensation mechanism, which is reflected in the charge–discharge profile. The initial charge process exhibits a characteristic voltage profile, with a potential slope of up to ~4.5 V and subsequent irreversible plateau at ~4.5 V^{1,26}. Based on X-ray absorption spectroscopy (XAS) studies, charge compensation can be achieved by the TM redox couple (e.g., the Ni²⁺/Ni⁴⁺ couple) during the voltage slope^{19,30–32}, corresponding to the shrinkage and expansion of the *a* and *c* parameters, respectively^{26–29}. In contrast, it is generally accepted that charge compensation can be achieved by oxygen (O^{2–}/O[–] couple and/or O₂ release) during the potential plateau, where the lattice parameters remain almost unchanged^{26–29,32–37}. Oxygen removal is consistent with an irreversible capacity loss observed during the initial charge–discharge cycle.

In terms of delithiation behavior of the single-phase structure model, Li ions should be uniformly extracted from the entire structure because the Li environment is homogeneous. In contrast, in the composite structure model, it would be expected that the Li ions are first extracted from the Ni²⁺-bearing LiMO₂ domain at the potential slope, and subsequently from the Li₂MnO₃ domain at the plateau region^{2,3}. However, previous studies have shown that Li ions are deintercalated from the Li₂MnO₃-like environment at potential slopes of <4.5 V^{24,38}. Recently, well-considered NMR shift assignments were reported for Li_{1.2}Ni_{0.18}Mn_{0.61}Mg_{0.01}O₂, where the local cationic configurations were compatible with the characteristic ⁷Li MAS NMR signals while satisfying local electroneutrality constraints³⁹. The structural evolution based on the changes in NMR signals during the first electrochemical cycle was also discussed, but the mechanism remains a source of debate due to the complicated spectral deconvolution including spinning sideband (SSB) manifolds in that study. Magic-angle turning phase-adjusted sideband separation (MATPASS) is a recently developed NMR technique and its sheared projection, pj-MATPASS spectrum, can provide well-resolved isotropic signals without the SSB manifolds⁴⁰. Subsequent studies have reported the delithiation/lithiation dynamics of different Li sites in various LMR cathodes (Li₂MnO₃, Li_{1.2}Ni_{0.2}Mn_{0.6}O₂, and Li_{1.2}Ni_{0.13}Co_{0.13}Mn_{0.54}O₂) using operando NMR and pj-MATPASS NMR techniques. These studies suggested that the Li ions in the TM layer were preferentially extracted during the first 20% of the charging and Li ions in both the Li and TM layers were subsequently removed at similar rates⁴¹. However, the detailed spectral evolutions of each signal component in the pj-MATPASS spectra were not discussed. Herein, synchrotron-radiation XRD, soft XAS, and pj-MATPASS NMR techniques were used to examine the delithiation behavior of a composite-structured Li_{1.2}Ni_{0.2}Mn_{0.6}O₂ in a semi-quantitative manner, and the sequential delithiation from the composite domains during the initial charge was demonstrated. The structural evolution after the initial charge–discharge cycle was also briefly discussed.

Results and discussion

Structural evolution of Li_{1.2}Ni_{0.2}Mn_{0.6}O₂ during the 1st charge–discharge cycle. Figure 1 shows the charge–discharge profiles of Li_{1.2}Ni_{0.2}Mn_{0.6}O₂ for the 1st, 2nd, and 20th cycles (complete profiles and corresponding dQ/dV curves are provided in Fig. S1). Sampling points for the structural analyses are clearly marked. Figure 2(a) shows the SR-XRD profiles for the 1st charge–discharge cycle. Based on single-phase notation, the pristine material was indexed with a space group of C2/m and the lattice parameters were refined as *a* = 4.951 Å, *b* = 8.558 Å, *c* = 5.028 Å, and β = 109.213° (#1)^{42,43}, although the high-angle annular dark field (HAADF)-STEM image of the material showed a composite structure, where the atomic columns of the TM layer of Li₂MO₃ and LiMO₂ are clearly discernible (Fig. S2(a))⁴². Close inspection of the strongest 001 diffraction peak provides clear suggestions regarding average crystal structure modification during the delithiation/lithiation process (Fig. 2(a), inset). The 001 peak moves to a lower 2θ value during charging to 100 mA h g⁻¹ (potential slope region, #2 and 3). At 200 mA h g⁻¹, at a midway point of the potential plateau region, the peak width broadens with a position close

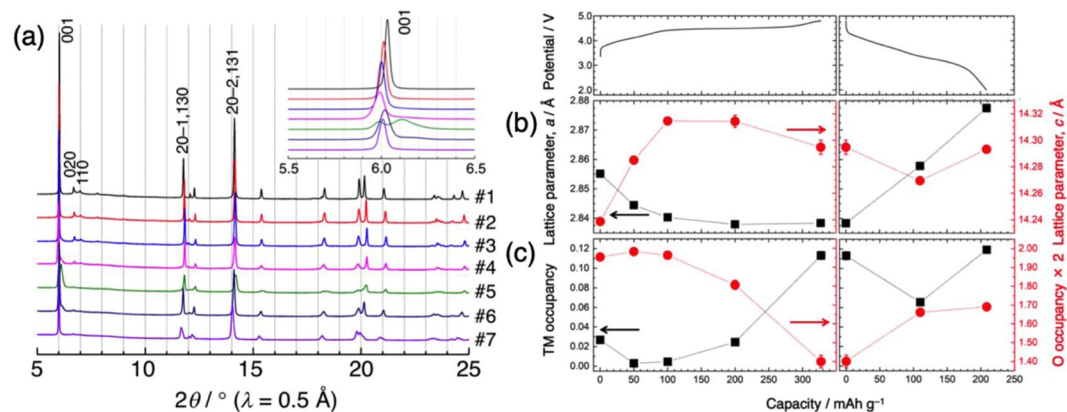


Figure 2. (a) SR-XRD profiles of the $\text{Li}_{1.2}\text{Ni}_{0.2}\text{Mn}_{0.6}\text{O}_2$ electrode at the 1st cycle. The strongest 001 diffraction peak was indexed with $C2/m$ and is enlarged in the inset. The sample numbers are described in Fig. 1. (b) Evolution of the a and c lattice parameters and (c) TM and O occupancies during the 1st cycle. Error bars in (b,c) indicate the standard uncertainties ($\pm 3\sigma$) derived from the Rietveld refinements (smaller than the symbols in most cases).

to that at 100 mA h g^{-1} (#4). Subsequently, the peak splits into two separate peaks at 4.8 V (#5), which then merge into a single peak during the lithiation, indicating that the structural modification is reversible (#6 and 7). A similar type of peak splitting at a high potential has been reported by Koga *et al.*, who attributed the two peaks at lower and higher 2θ to bulk and degraded surface phases, respectively⁴⁴. Herein, the peak at higher 2θ is close to the strongest 111 diffraction peak of the Li-poor cubic spinel $\text{Li}_{0.05}\text{Mn}_2\text{O}_4$ ($\lambda\text{-MnO}_2$, $a = 8.0445\text{ \AA}$)^{45,46}. The formation of a spinel structure upon charging was substantiated via electron microscopy techniques^{16,47,48}. The superlattice peaks characteristic of $C2/m$ were observed for the pristine material in the 2θ range of $6.3^\circ\text{--}11.0^\circ$. The intensity of these peaks gradually decreased during the delithiation process, which was mostly irreversible (Fig. S3). This indicates that the Li/TM honeycomb ordering in the TM layer was permanently lost by Li extraction from the original structure.

Rietveld refinements with the space group of $R\text{--}3m$ ($Fd\text{--}3m$ for the second phase at 4.8 V) were performed for simplicity, although the refinements with the $C2/m$ structure may yield better Reliability factors (R_p and R_{wp}). For the $R\text{--}3m$ structure, the oxygen occupancy at the $6c$ Wyckoff position and the TM ion occupancy in the Li and TM layers ($3a$ and $3b$ positions, respectively) with fixed isotropic atomic displacement parameters were refined in addition to the a and c lattice parameters. For the $Fd\text{--}3m$ structure, only the a lattice parameter was refined and the superlattice peaks in the 2θ range of $6.3^\circ\text{--}11.0^\circ$ were omitted during the refinement procedures. The final R_p and R_{wp} values were $<4.6\%$ and $<7.0\%$, respectively, for all samples. Figure 2(b) shows the variations of the a and c parameters during the 1st cycle where a decreases and c increases over the potential slope region. The contraction of the a -axis and elongation of the c -axis are a consequence of Ni oxidation, forming smaller ionic radii and increasing electrostatic repulsion between the close-packed oxygen layers due to Li extraction^{26–29,44}. In contrast, the variations of the lattice parameters were negligible during the potential plateau region, suggesting charge compensation by the oxygen redox mechanism^{26–29,44}. The nanoscale phase separation from the composite layered structure to layered and spinel(-like) structures was observed only at 4.8 V and the mass ratio of the two phases was estimated as 66:34 from the refinement. Recently, it was reported that phase separation at high voltage is dependent on particle size²⁹ where two-phase behavior was observed in samples with large particles ($10\text{ }\mu\text{m}$), but one-phase behavior was found for samples with sub-micrometer particles. Herein, the sample exhibited a $\sim 5\text{ }\mu\text{m}$ secondary particle size, so phase separation was observed. During the lithiation process, the a parameter largely increases, while the c parameter slightly decreases. The former is associated with reduction of the TM ions, and the latter is likely due to incomplete lithium uptake. Figure 2(c) shows the TM ion occupancy variations in the Li layer for the $R\text{--}3m$ structure, suggesting increased TM migration into the Li layer after activation. Spectroscopic evidence of the migration was also provided by resonant X-ray diffraction spectroscopy (RXDS)⁴⁹. The variation of oxygen occupancy is also shown in Fig. 2(c). Oxygen atoms exhibit relatively weak X-ray scattering power compared to TM atoms, but the high resolution and high flux X-ray beam provided a general trend for oxygen occupancy in the refinement results. The oxygen occupancy remained nearly constant during the potential slope region, but decreased in the plateau region, suggesting oxygen loss from the layered structure. The oxygen loss and TM migration was correlated as the oxygen vacancy may facilitate TM migration⁵⁰. These results indicate that the layered structure retained at 4.8 V is highly defective, which may transform into a spinel-like structure with further delithiation. The oxygen occupancy is partially recovered during lithiation. A similar behavior was previously reported, and it is considered that the oxygen vacancies are partly refilled by extracting the oxygen from surface film components (for example, Li_2CO_3) on the particle, which are caused by electrolyte decomposition⁵¹. Alternatively, the peroxide moiety formed in the charged material may account for the reversibility of oxygen occupancy⁵¹. Such O-O dimer species locate at the interstitial positions, which are not explicitly taken into account for structural refinements. Li reinsertion breaks the dimer bond, and the oxygen atoms may go back to the $6c$ site in the discharged material. A possibility of the formation of peroxide species is discussed in the next section.

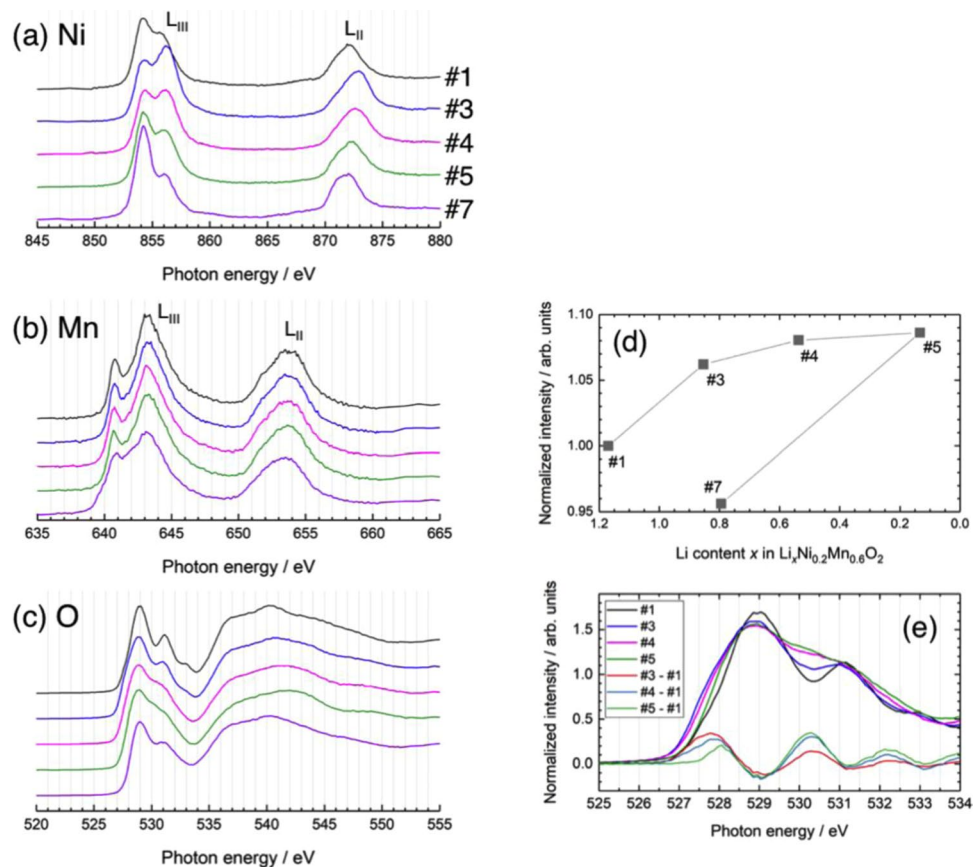


Figure 3. (a) Ni L-, (b) Mn L-, and (c) O K-edge XAS spectra of the $\text{Li}_{1.2}\text{Ni}_{0.2}\text{Mn}_{0.6}\text{O}_2$ electrode at the 1st cycle. (d) Evolution of the integrated intensity in the pre-edge region of the O K-edge XAS spectra. (e) Difference spectra of the pre-edge region of the O K-edge XAS spectra.

Figure 3 shows the Ni, Mn $L_{II,III}$, and O K-edge XAS spectra acquired in partial fluorescence yield (PFY) or inverse partial fluorescence yield (IPFY) mode for the 1st cycle. The TM L-edge XAS directly probes the electron dipole transition from the 2p core level to 3d unoccupied states and is sensitive to the valence and coordination states. The L-edge spectra split into L_{III} and L_{II} lines due to the spin-orbit interaction of $2p_{3/2}$ and $2p_{1/2}$ core electrons. The Ni L_{III} -edge spectrum of the pristine sample (#1) was similar in shape to those of NiO and LiNiO_2 ^{32,52,53}. The average Ni valence was determined to be 2.3+ from the Ni K-edge XAS spectrum⁴⁹. At the end of the potential slope region, the lower energy peak of the L_{III} -edge decreased in intensity while the higher energy peak increased, with the L_{II} -edge peak shifting to a higher energy, indicating an increase in Ni oxidation state (#3). However, the higher energy peak of the L_{III} -edge decreased in relative intensity, while the L_{II} -edge peak shifted back to a lower energy at the potential plateau, suggesting partial reduction of Ni (#4 and 5). The L_{III} -edge spectrum of the sample discharged to 2.0 V (#7) was almost identical to that of NiO, indicating a valence state close to 2+. From the spectral analysis by the linear combination fitting, in which it was assumed that spectra #3 and #7 are representative of Ni^{4+} and Ni^{2+} states, respectively, the Ni valence state was estimated to be 3+ at 4.8 V (Table S1). The decreased Ni valence state at high voltages has been previously reported by several researchers^{32,54}. Hy *et al.* suggested that this reduction behavior was associated with the preferential hybridization of Ni with activated oxygen species formed at high potentials⁵⁴. The Mn L_{III} -edge spectrum of the pristine material resembled that of Li_2MnO_3 ^{54–56}, indicative of the tetravalent state, as expected (Fig. 3(b)). The oxidation state of Mn remained almost constant during charging, in contrast to previous studies of Li_2MnO_3 , where the valence state was reduced to 3.5+ at 4.8 V^{55,56}. This also departs from the decreased Ni valence mentioned above. Ni has a larger electronegativity and is expected to strongly hybridize with the activated oxygen species preferentially over the Mn ion⁵⁴. In contrast, Mn valence decreased to 3.5+ at 2.0 V, based on the spectral analysis using reference spectra of MnO (Mn^{2+}), Mn_2O_3 (Mn^{3+}), and Li_2MnO_3 (Mn^{4+}) (Table S1). The O K-edge spectra showed pre-edge peaks between 527 and 534 eV and a white line above 534 eV, which come from the O 2p unoccupied states hybridized with TM 3d and 4s,p states, respectively (Fig. 3(c)). Detailed examination indicated that the spectral intensity of the pre-edge area changes in two steps during charging and its intensity evolution between 525 and 534 eV is plotted in Fig. 3(d). The intensity increased during the potential slope but remained nearly constant over the plateau region. The difference spectra between spectra #1, #3, and #5 are provided in Fig. 3(e). An intensity increase at the lower energy side (~528 eV) of the 529 eV peak was observed until the end of the potential slope³⁶. This was also observed in the O K-edge spectrum for $\text{Li}_{1-x}\text{MO}_2$ and was attributed to the increased contribution of the ligand hole in the LiMO_2 domain^{54,57–61}. This spectral change is associated with a valence increase of Ni ions

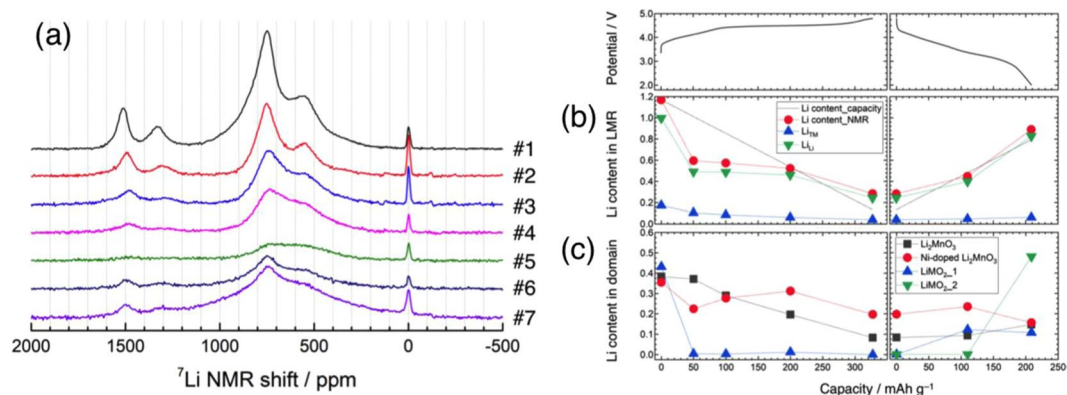


Figure 4. (a) ^7Li pj-MATPASS NMR spectra of the $\text{Li}_{1.2}\text{Ni}_{0.2}\text{Mn}_{0.6}\text{O}_2$ electrode at the 1st cycle. (b) Evolution of the total Li content derived from the ^7Li NMR intensity (Li_{TM} and Li_{Li}) and electrochemical measurements. (c) Evolution of Li contents in the various domains (Li_2MnO_3 -, Ni-doped Li_2MnO_3 -, and LiMO_2 -like domains) during the 1st cycle.

hybridized with O ions, suggesting a cation-anion dual charge compensation process⁴³. The 528 eV component decreased at 4.8 V, and a new peak at ~ 530 eV increased in intensity. The former behavior is due to the valence decrease of Ni, as shown in the Ni L_{III} -edge spectra, while the latter is unrelated to the valence change of the TM ions in the LiMO_2 domain and is instead related to Li_2MnO_3 domain structural changes. Previous studies reported a similar intensity increase at 530 eV for delithiated Li_2MnO_3 ^{55,56}. This is consistent with the assertion that Li ions are extracted from the Li_2MnO_3 domain over the potential plateau^{2,3}. The intensity increase at 530 eV likely corresponds to the formation of peroxide-like oxygen in the Li_2MnO_3 domain, because the peak position is similar to that of Li_2O_2 ^{33,55,62}. Moreover, a recent study examined the O-O vibrational mode typical of the peroxide moiety in the charged $\text{Li}_{1.2}\text{Ni}_{0.2}\text{Mn}_{0.6}\text{O}_2$ using *in situ* surface-enhanced Raman scattering (SERS)⁶³. Upon discharge, the spectral features in the pre-edge region were similar to those of pristine material, indicating that the electronic states of O ions were mostly recovered.

Figure 4(a) shows the pj-MATPASS NMR spectra of $\text{Li}_{1.2}\text{Ni}_{0.2}\text{Mn}_{0.6}\text{O}_2$ electrodes during the 1st cycle. A comparison of NMR spectra of the pristine material, acquired using different techniques and under different experimental conditions, shows that only the pj-MATPASS spectrum provides isotropic signals without SSB manifolds even at a moderate sample spinning rate of 30 kHz and high magnetic field of 14.1 T (Fig. S4). The ^7Li signals for $\text{Li}_{1.2}\text{Ni}_{0.2}\text{Mn}_{0.6}\text{O}_2$ were split into 6 pseudo-Voigt components (Fig. S5). There are different local environments, and some components are correlated with each other, suggesting that these local environments are attributable to different phases (domains) in $\text{Li}_{1.2}\text{Ni}_{0.2}\text{Mn}_{0.6}\text{O}_2$. Based on previous studies, where the additive nature of the Fermi contact shift and local cationic configurations (bond angles of Li-O-TM) were summed^{39,64}, each component was assigned. The predominant peak components at 749 and 1514 ppm were exclusively assigned to Li ions in the Li and TM layers of the Ni-free Li_2MnO_3 -like region in $\text{Li}_{1.2}\text{Ni}_{0.2}\text{Mn}_{0.6}\text{O}_2$, respectively. These components were close to those of Li_2MnO_3 ^{41,56}, and additional signals appeared with increasing Ni contents in $\text{Li}[\text{Li}_{(1-2x)/3}\text{Ni}_x\text{Mn}_{(2-x)/3}]\text{O}_2$ (Fig. S6). The peak components at 553 and 1331 ppm were attributed to Li ions in the Li and TM layers of the Ni-doped Li_2MnO_3 -like region, respectively^{24,25,64}. The latter Li ions are surrounded by 6 TM ions in Ni:Mn = 1:5 in the TM layer. Because Ni ions in an octahedral environment exhibit lower spins ($S = 1, 1/2$, and 0 for Ni^{2+} , Ni^{3+} , and Ni^{4+} , respectively) compared to $S = 3/2$ for Mn^{4+} , yielding weaker hyperfine interactions, the ^7Li signals in the Ni-doped Li_2MnO_3 ($\text{Li}_2[\text{Ni}_{1/6}\text{Mn}_{5/6}]\text{O}_3$ -like) domain appeared at lower frequencies (553 and 1331 ppm) compared to those in the Ni-free domain (749 and 1514 ppm)⁶⁴. The 791 ppm component was tentatively assigned to the ^7Li signal from the Ni-containing LiMO_2 domain due to the lack of the corresponding ^7Li signal from the TM layer. Some assignments differed from those in a recent study³⁹, where the peaks at 576 and 946 ppm (corresponding to the peaks at 553 and 791 ppm observed herein) were assigned oppositely. The remaining 352 ppm component was not observed in previous studies^{39,64}, and was tentatively ascribed to Li ions in the Li layer of the $\text{Li}_2[\text{Ni}_{2/6}\text{Mn}_{4/6}]\text{O}_3$ -like domain. This contribution is negligible and is merged with the discussion of the 553 ppm peak below. Finally, the sharp signal at 0 ppm arises from impurity phases such as Li_2CO_3 and organic lithium salts.

The HAADF-STEM images visualized that the atomic columns of the TM layer characteristic of Li_2MO_3 and LiMO_2 -like structure were alternately stacked over several nm (Fig. S2(a))⁴². This indicates that $\text{Li}_{1.2}\text{Ni}_{0.2}\text{Mn}_{0.6}\text{O}_2$ consists of composite domains adopting Li_2MO_3 - and LiMO_2 -based layered structures. The ^7Li pj-MATPASS spectra provided detailed information about chemical composition of the composite domains in $\text{Li}_{1.2}\text{Ni}_{0.2}\text{Mn}_{0.6}\text{O}_2$. The ratio of Li ions in the Li and TM layers, $\text{Li}_{\text{TM}}/\text{Li}_{\text{Li}}$, was estimated from the ^7Li pj-MATPASS spectrum for the pristine material (0.17). Therefore, the bulk chemical composition of the pristine material was re-expressed as $\text{Li}[\text{Li}_{0.17}\text{Ni}_{0.21}\text{Mn}_{0.59}]\text{O}_2$ (almost identical to that of $\text{Li}_{1.2}\text{Ni}_{0.2}\text{Mn}_{0.6}\text{O}_2$) including the Ni and Mn valence states estimated from previous XAS results (2.3+ and 4+, respectively)⁴⁹. The composition and ratio of the Ni-free and Ni-doped Li_2MnO_3 ($\text{Li}_{1.33}\text{Mn}_{0.67}\text{O}_2$) and LiMO_2 domains were estimated as $0.28\text{Li}_{1.37}\text{Mn}_{0.63}\text{O}_{2(-\delta)}$ (similar to $\text{Li}_{1.33}\text{Mn}_{0.67}\text{O}_2$), $0.28\text{Li}_{1.26}\text{Ni}_{0.11}\text{Mn}_{0.57}\text{O}_2$, and $0.43\text{LiNi}_{0.41}\text{Mn}_{0.57}\text{O}_2$, considering the experimental ^7Li signal ratio $\text{Li}_{\text{TM}}/\text{Li}_{\text{Li}}$ of each domain (0.37, 0.26, and 0, respectively), and cation vacancies as well as the assumption that

the Ni ions are tetravalent in the Ni-doped Li_2MnO_3 -like domain with Ni:Mn = 1:5 (see also Supplementary Information). The estimated phase ratio is comparable to the composite notation of $\text{Li}_{1.2}\text{Ni}_{0.2}\text{Mn}_{0.6}\text{O}_2$, $0.6\text{Li}_{1.33}\text{Mn}_{0.67}\text{O}_2$ - $0.4\text{LiNi}_{0.5}\text{Mn}_{0.5}\text{O}_2$. It should be emphasized that the Ni-doped Li_2MnO_3 -like domain, $\text{Li}_{1.26}\text{Ni}_{0.11}\text{Mn}_{0.57}\text{O}_2$, is a dominant component in the material, acting as a boundary buffer phase between the Li_2MnO_3 and LiMO_2 domains³⁹. The composition and ratio of these domains differed from those estimated in ref. 39 with a similar bulk composition, $\text{Li}_{1.2}\text{Ni}_{0.18}\text{Mn}_{0.61}\text{Mg}_{0.01}\text{O}_2$, mostly due to different peak assignments. It should be noted that the composite structure of differently composed domains in $\text{Li}_{1.2}\text{Ni}_{0.2}\text{Mn}_{0.6}\text{O}_2$ may introduce chemical inhomogeneity within a nanoscale particle. The inhomogeneous Ni distribution relative to Mn and O is highlighted in the energy-dispersive X-ray spectrometry (EDS) mapping images of a single particle (Fig. S2(b)). The $\text{LiNi}_{0.41}\text{Mn}_{0.57}\text{O}_2$ domain may be concentrated in the Ni-rich region.

The ^7Li pJ-MATPASS and its difference spectra indicate that Li extraction from each signal component is not constant (Figs. S5 and S7). Figure 4(b) shows the integrated intensity variation of ^7Li signals of $\text{Li}_{1.2}\text{Ni}_{0.2}\text{Mn}_{0.6}\text{O}_2$ for the 1st cycle (see Fig. S8 for each component). Herein, the NMR-based composition, $\text{Li}[\text{Li}_{0.17}\text{Ni}_{0.21}\text{Mn}_{0.59}]\text{O}_2$ (theoretical capacity: $369.5 \text{ mA h g}^{-1}$), was used instead of the ICP-AES-based composition, $\text{Li}_{1.25}\text{Ni}_{0.20}\text{Mn}_{0.55}\text{O}_{2-\delta}$, or the ideal composition, $\text{Li}_{1.2}\text{Ni}_{0.2}\text{Mn}_{0.6}\text{O}_2$, for consistency. Total ^7Li signals decreased in intensity during charging. It should be noted that the Li contents at 50 and 100 mA h g^{-1} were significantly underestimated compared to those calculated from the delivered current densities and similar behaviors were reported for LiCoO_2 and $\text{LiNi}_{0.5}\text{Mn}_{1.5}\text{O}_4$ ^{65,66}. This abrupt intensity reduction during the early stages of delithiation arises from the localized nature of the electrons on paramagnetic ions and nearby Li^+ ions, causing rapid relaxation of all nearby ^7Li nuclear spins before signal acquisition. In contrast, the Li content in the sample at 4.8 V was slightly overestimated, indicating that the delivered charging capacity includes some contribution from side reactions such as electrolyte decomposition at high potentials. During discharging, the Li contents increased almost linearly. Figure 4(b) shows that the Li ions were extracted from the Li and TM layers of $\text{Li}[\text{Li}_{0.17}\text{Ni}_{0.21}\text{Mn}_{0.59}]\text{O}_2$. The $\text{Li}_{\text{TM}}/\text{Li}_{\text{Li}}$ ratio remained almost constant during charging, but decreased gradually during discharging (Fig. S9). This suggests that the Li ions cannot easily be reinserted into the TM layer of the discharged material.

The Li content in each domain during the 1st charge–discharge cycle is plotted in Fig. 4(c). The LiMO_2 domain content is drastically reduced at the 50 mA h g^{-1} charge, leading to the abrupt intensity reduction discussed above (Fig. 4(b)). Therefore, it is clear that Li ions are preferably extracted from the LiMO_2 domain over the potential slope region. From the XAS results (Fig. 3(a) and ref. 49), Li extraction is electronically compensated by the valence increase of Ni in the LiMO_2 domain. It should be noted that some ^7Li signals were lost in the Ni-free and Ni-doped Li_2MnO_3 domains over the potential slope region (Figs. 4(a) and S7). This signal loss is likely fictitious, resulting from the strong interaction with the localized paramagnetic spins in the nearby LiMO_2 domain. Li ions are subsequently deintercalated from the Li_2MnO_3 domain during the potential plateau with charge compensation via oxidation of lattice oxygen and O_2 release, as described above. At 4.8 V, a broad ^7Li signal remained at $\sim 600 \text{ ppm}$ (Fig. 4(a), #5), suggesting that Li ions are mainly retained in the disordered Li layer of the Ni-doped Li_2MnO_3 domain. It should be noted that some researchers have attributed the broad signal at 500–600 ppm to Li ions at tetrahedral sites^{38,64}. Considering the phase separation observed in the XRD profile at 4.8 V (Fig. 2(a)), delithiation from the Li_2MnO_3 domain involves the oxygen loss and the formation of a spinel-like phase⁵⁶, and the remaining Li ions are most likely retained in the layered structure consisting of the Ni-doped Li_xMnO_3 domain. The composition of the material at 4.8 V was determined to be $\text{Li}_{0.24}[\text{Li}_{0.04}\text{Ni}_{0.21}\text{Mn}_{0.59}]\text{O}_{2-\delta}$. During discharging, Li ions are mainly reinserted into the LiMO_2 domain and a new broad component appears when discharged to 2.0 V (Fig. S7). This was ascribed to a ^7Li signal from a newly formed LiMO_2 phase, where the Ni and Mn ions in the TM layer are randomly distributed in various configurations. This new phase becomes dominant and the spectrum of the discharged material at 2.0 V differed significantly from that of the pristine material. The chemical composition at 2.0 V can be expressed as $\text{Li}_{0.83}[\text{Li}_{0.06}\text{Ni}_{0.21}\text{Mn}_{0.59}]\text{O}_{2-\delta}$ while the ideal composition would be $\text{Li}_{-1.0}\text{Ni}_{0.25}\text{Mn}_{0.75}\text{O}_2$ (expected reaction: $\text{Li}_{1.2}\text{Ni}_{0.2}\text{Mn}_{0.6}\text{O}_2 \rightarrow 0.8\text{LiNi}_{0.25}\text{Mn}_{0.75}\text{O}_2 + 0.4\text{Li} + 0.2\text{O}_2 \uparrow$, where the oxygen loss was evidenced in Fig. 2(c)). These results indicate that delithiation proceeds sequentially from the LiMO_2 and Li_2MO_3 domains in the $\text{Li}_{1.2}\text{Ni}_{0.2}\text{Mn}_{0.6}\text{O}_2$ composite structure. This non-uniform Li extraction from the composite material was demonstrated for $\text{Li}_{1.2}\text{Mn}_{0.4}\text{Fe}_{0.4}\text{O}_2$ by elemental mapping analyses of electron energy loss spectroscopy (EELS)-STEM images⁶⁷. The structure of $\text{Li}_{1.2}\text{Ni}_{0.2}\text{Mn}_{0.6}\text{O}_2$ after the initial cycle changed to a domainless single phase LiMO_2 , although some Li_2MnO_3 domain remained, indicating that irreversible structural changes occur during the initial charge–discharge process.

The ^7Li signal at 1514 ppm is relatively sharp and well separated from other components, allowing the peak position changes to be confirmed with high confidence (Fig. S10). Over the potential slope region, the peak position shifted towards lower frequencies corresponding to the Ni valence increase. The valence state of Ni in the LiMO_2 domain changed from Ni^{2+} ($S = 1$) to Ni^{4+} ($S = 0$), reducing the Fermi contact interaction and shifting the peak position to lower frequencies. In contrast, no peak shift was observed over the potential plateau region, indicating that the TM ions were not involved in charge compensation. During the discharging process, the peak position returns, to some extent, to higher frequencies due to TM ion reduction. These changes are qualitatively consistent with that of the a lattice parameter.

Therefore, it can be concluded that the irreversible potential plateau in the initial charge–discharge cycle corresponds to a structural change (i.e., structural activation) from a composite structure of Li_2MO_3 and LiMO_2 domains to a single-phase (domainless) structure. This is associated with cation mixing (i.e., migration of TM ions) during the formation of a spinel-like structure at a high potential. Upon back-transformation to a layered structure during discharging, the TM ions move back to positions different from their original positions in the TM layer, and the TM ions are uniformly dispersed, resulting in a domainless structure.

Structural evolution after the initial charge–discharge cycle. The structure of $\text{Li}_{1.2}\text{Ni}_{0.2}\text{Mn}_{0.6}\text{O}_2$ after the initial charge–discharge cycle will be briefly discussed. The charge–discharge profiles for the 2nd and 20th

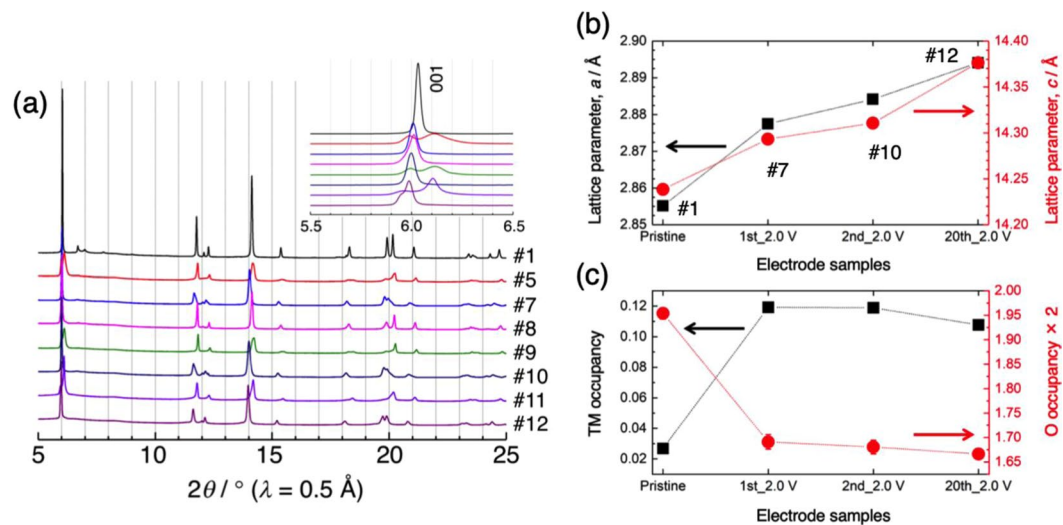


Figure 5. (a) SR-XRD profiles of the $\text{Li}_{1.2}\text{Ni}_{0.2}\text{Mn}_{0.6}\text{O}_2$ electrode at the 1st, 2nd, and 20th cycles. The strongest 001 diffraction peak is enlarged in the inset. (b) Evolution of the a and c lattice parameters and (c) TM and O occupancies for the pristine, 1st, 2nd, and 20th discharged samples. Error bars in (b,c) indicate the standard uncertainties ($\pm 3\sigma$) derived from the Rietveld refinements (smaller than the symbols in most cases).

cycles are shown in Fig. 1. The capacity fade was small but gradual voltage fading was observed up to the 20th cycle (Fig. S1). The charging and discharging capacities at the 20th cycle were 218.8 and 216.8 mA h g^{-1} , respectively.

The SR-XRD profiles of the fully charged and discharged samples at the 1st, 2nd, and 20th cycles are shown in Fig. 5(a). The diffraction profiles of the 2nd charged and discharged samples (#9 and 10) are quite similar to those of the 1st cycle (#5 and 7). Even at the 20th charge–discharge cycle, the 001 diffraction peak of the charged sample was split (see Fig. 5(a), inset), merging into a single peak for the discharged sample (#11 and 12). We note that each peak at lower and higher 2θ of the split 001 diffraction peak in the 20th charged sample was broader and narrower, respectively, than the corresponding peaks in the 1st and 2nd charged samples. This may indicate the decrease in domain size (or crystallinity) of layered structure phase and the increase in domain size (or crystallinity) of spinel phase. In addition, a small shoulder at the lower 2θ side of the 001 diffraction peak in the 20th discharged sample may be a remnant peak of the layered structure observed in the charged state. These results indicate that the structural changes are reversible after structural activation during the initial cycle. This structural stability is significantly different from that of Li_2MnO_3 , which changes from a layered structure to a highly disordered spinel-like structure in 20 cycles⁵⁶. It should be noted that the spinel-like phase was observed at 4.8 V in the 20th cycle, although the Li_2MnO_3 domain completely disappeared, as discussed below. Therefore, this spinel-like structure results from the domainless layered structure at the high voltages⁶⁸. Figure 5(b) shows the lattice parameters changes of the pristine and discharged samples at the 1st, 2nd, and 20th cycles. The domain structure in the pristine material changes to a domainless structure after the 1st discharge and both the a - and c -axes were correspondingly expanded. The lattice parameters further increased for the 2nd and 20th discharged materials. The extent of TM ion migration (to the Li layer) and oxygen site occupancy remained nearly constant after the 1st cycle (Fig. 5(c)). Therefore, the increases in a - and c -axes are likely caused by the decreased average oxidation state of TM ions and decreased Li content, respectively.

Figure 6 shows the Ni and Mn $L_{II,III}$ -edge XAS spectra for the 1st, 2nd, and 20th charged and discharged samples. The Ni valence was divalent for all discharged materials. The Ni valence was estimated to be 3.0+ and 2.6+ in the 2nd and 20th charged materials, respectively (Table S1). The average Mn valence in the pristine and 1st, 2nd, and 20th discharged states gradually decreased from 4.0+ to 3.5+, 3.4+, and 3.3+, respectively (Table S1), which is consistent with increased a -axis, indicating that Mn ions are redox active after the initial cycle. This is consistent with a previous study using hard X-ray photoelectron spectroscopy (HAXPES)⁴³, while these soft XAS spectra include some contributions from the active material surface degradation. The present results suggest that Ni ions become redox inactive at higher voltages ($> \sim 3.2 \text{ V}$ for $\text{Ni}^{2+}/\text{Ni}^{4+}$ redox couple), and Mn ions become redox active at lower voltages ($< \sim 3.2 \text{ V}$ for $\text{Mn}^{3+}/\text{Mn}^{4+}$ redox couple) during repeated cycles. This is involved in voltage fading behavior shown in Fig. S1(b).

Figure 7(a) shows the ^7Li p -MATPASS spectra of the 1st, 2nd, and 20th charged and discharged samples, where comparison of the charged (#5, 9, and 11) and discharged samples (#7, 10, and 12) shows no significant differences in the spectra, except for consumption of the residual signals of the Li_2MnO_3 component at the 20th cycle. Therefore, the Li ions were reversibly extracted and inserted into the domainless layered structure after the initial cycle. Broad signals centered at 585 and 630 ppm were observed in the 20th charged and discharged materials, respectively. The higher frequency isotropic shift corresponds to the lower average oxidation state of TM ions, with higher spin numbers of $S = 2$ and 1 (for Mn^{3+} and Ni^{2+} , respectively) compared to $S = 3/2$ and 0 (for Mn^{4+} and Ni^{4+} , respectively). The Li contents estimated from the signal intensities of the 20th charged and discharged samples were slightly overestimated relative to that calculated from the charging and discharging capacities

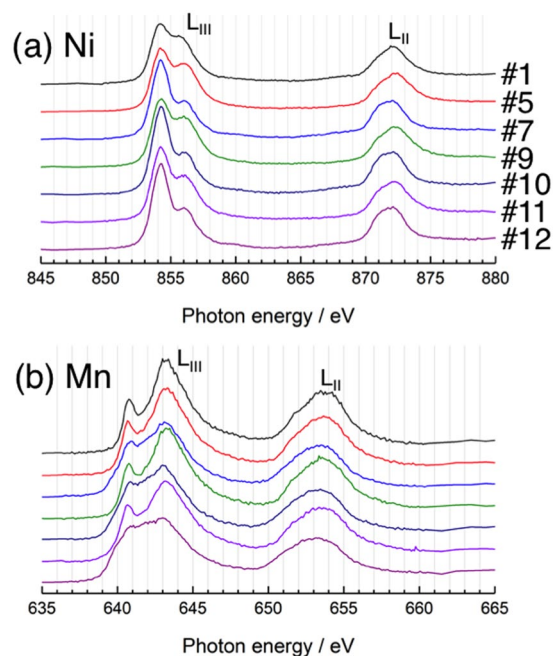


Figure 6. (a) Ni L- and (b) Mn L-edge XAS spectra of the $\text{Li}_{1.2}\text{Ni}_{0.2}\text{Mn}_{0.6}\text{O}_2$ electrode at the 1st, 2nd, and 20th cycles.

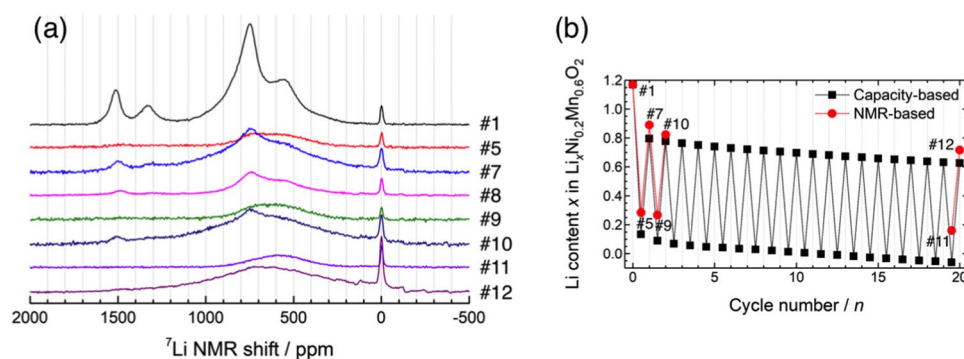


Figure 7. (a) ^7Li pj-MATPASS NMR spectra of the $\text{Li}_{1.2}\text{Ni}_{0.2}\text{Mn}_{0.6}\text{O}_2$ electrode at the 1st, 2nd, and 20th cycles. (b) Evolution of the total Li content derived from the ^7Li NMR intensity and electrochemical measurements up to 20th cycle.

(Fig. 7(b)). Li ions were observed in $\text{LiNi}_{0.25}\text{Mn}_{0.75}\text{O}_2$ in the 20th charge (#11), although the Li content calculated from the capacity at 4.8 V should be empty. These results indicate that the long-cycled charge–discharge capacity includes significant contributions from accumulative side reactions and that NMR spectroscopy is a reliable tool for directly measuring the Li content in active materials.

Conclusions

Based on the composite structure concept of LMRs, the delithiation behavior of $\text{Li}_{1.2}\text{Ni}_{0.2}\text{Mn}_{0.6}\text{O}_2$ was reexamined during charge–discharge cycles. It was confirmed that the pristine material contains a composite layered structure composed of Li_2MO_3 and LiMO_2 nanoscale domains using electron microscopy (HAADF-STEM). Solid-state NMR further provided a quantitative information about the composite structure (i.e., composition and ratio of the domains), which consists of pure Li_2MnO_3 , $\text{Li}_2[\text{Ni}_{1/6}\text{Mn}_{5/6}]\text{O}_3$, and $\text{Li}[\text{Ni},\text{Mn}]\text{O}_2$ nanoscale domains. We found that Li ions are sequentially and inhomogeneously extracted from the composite structure. Li ions were deintercalated from the $\text{Li}[\text{Ni},\text{Mn}]\text{O}_2$ domain in the potential slope region during initial charging, where the Ni ions were redox active for charge compensation. Subsequently, Li ions were preferably extracted from both the Li and TM layers in the Li_2MnO_3 domain in the potential plateau region at a high voltage, where the charge was compensated by oxygen anions by formation of ligand holes, peroxide-like moieties, or O_2 release. Li ions mostly remained in the Li layer of the $\text{Li}_2[\text{Ni}_{1/6}\text{Mn}_{5/6}]\text{O}_3$ domain at 4.8 V. The XRD profiles indicated a reversible phase separation into layered rock-salt and spinel-like nanodomain structures at 4.8 V, where the latter phase is

associated with TM ion migration from the TM layer into the vacant Li layer in the Li_2MnO_3 domain. During Li intercalation into the structure, cation remigration and mixing formed a domainless layered structure, and the active material became a single $\text{Li}[\text{Ni}_{0.25}\text{Mn}_{0.75}]\text{O}_2$ phase with a small content of remnant Li_2MnO_3 domain. After the 1st charge–discharge cycle, when irreversible structural activation occurred, the bulk structure showed reversible Li extraction accompanied by reversible lattice changes and phase separation into layered and spinel-like phases at high potentials. These results provide a new insight into the delithiation/lithiation behavior of nanoscale composite-structured LMRs, which further serve as understanding of the capacity and voltage fading mechanism relating to structural degradation of these materials.

Experimental methods

$\text{Li}_{1.2}\text{Ni}_{0.2}\text{Mn}_{0.6}\text{O}_2$ was synthesized via solid-state reaction at 900 °C for 12 h with the starting materials, $\text{LiOH} \cdot \text{H}_2\text{O}$, Ni_2CO_3 (Wako Pure Chemical Industries) and MnCO_3 (Kojundo Chemical Laboratory)^{42,43}. From scanning electron microscopy (SEM) observations, the average particle size was estimated to be $\sim 5 \mu\text{m}$, composed of an aggregate of small crystallites ($\sim 200 \text{ nm}$ in diameter). The chemical composition of the obtained material was determined to be $\text{Li}_{1.25}\text{Ni}_{0.20}\text{Mn}_{0.55}\text{O}_{2-\delta}$ ($\delta \approx 0.07$) via inductively coupled plasma-atomic emission spectrometry (ICP-AES; ICPS-8100, Shimadzu) and iodometric titration measurement that estimates the average oxidation state of the transition metals.

A positive electrode was prepared using a mixture of the active material, acetylene black (Denki Kagaku Kogyo), and polyvinylidene difluoride (PVDF, Kureha) at a weight ratio of 80:10:10 spread onto an aluminum foil with 1-methyl-2-pyrrolidone (NMP) and dried at 80 °C under vacuum overnight.^{43,56} The electrode was pressed to a thickness of 30–35 μm and foils of metallic lithium (0.2 mm in thickness, >99.9%, Honjo Metal) were used as counter and reference electrodes. These components were assembled with the Celgard 2500 separator and soaked in an electrolyte solution, and sealed in an aluminum-coated laminate-type cell in an Ar-filled glove box. The electrolyte solution used herein was 1 M LiPF_6 solution dissolved in anhydrous ethylene carbonate (EC) and ethylmethyl carbonate (EMC) at a volumetric ratio of 3:7 (Kishida Chemical).

The electrochemical measurements were performed at 50 °C on an automatic cycling and data recording system (HJ1001SD8, Hokuto Denko). The cells were galvanostatically cycled between 2.0 and 4.8 V vs. Li/Li^+ at a current rate of 20.5 mA g^{-1} .⁵⁶ The cells were carefully disassembled at the desired charge/discharge states in the glove box and rinsed with dimethyl carbonate (DMC) to remove any electrolyte solution residue.

Synchrotron-radiation XRD (SR-XRD) measurements were performed using powdered samples sealed in 0.5 mm ϕ borosilicate glass capillaries in the 2θ range of 4.0–52.7° with $\Delta\theta$ of 0.0025° at the BL28XU beamline in SPring-8 (Hyogo, Japan). An incident radiation of $\lambda = 0.4997 \text{ \AA}$ was used, which was calibrated with the lattice parameters of CeO_2 . The Rietveld refinements of the crystal structure parameters were performed using Jana2006⁶⁹.

Soft XAS measurements were performed at beamline BL-11 in the SR Center, Ritsumeikan University (Shiga, Japan). The samples were placed into a sample holder in the glove box and transferred using a transfer vessel to the high vacuum sample chamber without exposure to the air. The Ni, Mn $L_{II,III}$ -edge, and O K-edge spectra were acquired in partial fluorescence yield (PFY) mode. Mn $L_{II,III}$ -edge spectra were also acquired in inverse partial fluorescence yield (IPFY) mode to account for self-absorption effects⁷⁰. The PFY/IPFY spectra are (relatively) bulk-sensitive with a probing depth of up to $\sim 200 \text{ nm}$ ⁷¹.

^7Li MAS NMR spectra were acquired using an ECA-600 spectrometer (JEOL RESONANCE Inc.) at a magnetic field of 14.1 T with a wide-bore T3 MAS probe (Agilent Technologies). The powder samples were packed into 1.6 mm ϕ MAS ZrO_2 rotors with airtight caps in a glove box and spun at a spinning rate of 30 kHz during the experiments. The practical temperatures of the spinning samples at 30 kHz were estimated to be $\sim 60 \text{ °C}$ due to frictional heating. To obtain high resolution spectra, the pj-MATPASS technique⁴⁰ was used with a $\pi/2$ pulse width of 1.1 μs and a relaxation delay of 0.1 s. All spectra were referenced to a 1 M LiCl solution at 0.0 ppm. The signal intensities were normalized by the sample weight in the rotors.

Received: 11 December 2019; Accepted: 20 May 2020;

Published online: 22 June 2020

References

- Lu, Z., MacNeil, D. D. & Dahn, J. R. Layered Cathode Materials $\text{Li}[\text{Ni}_x\text{Li}_{(1/3-2x/3)}\text{Mn}_{(2/3-x/3)}]\text{O}_2$ for Lithium-Ion Batteries. *Electrochem. Solid-State Lett* **4**, A191–194, <https://doi.org/10.1149/1.1407994> (2001).
- Thackeray, M. M., Johnson, C. S., Vaughey, J. T., Li, N. & Hackney, S. A. Advances in manganese-oxide ‘composite’ electrodes for lithium-ion batteries. *J. Mater. Chem.* **15**, 2257–2267, <https://doi.org/10.1039/b417616m> (2005).
- Thackeray, M. M. *et al.* Li_2MnO_3 -stabilized LiMO_2 (M = Mn, Ni, Co) electrodes for lithium-ion batteries. *J. Mater. Chem.* **17**, 3112–3125, <https://doi.org/10.1039/b702425h> (2007).
- Ohzuku, T., Nagayama, M., Tsuji, K. & Ariyoshi, K. High-capacity lithium insertion materials of lithium nickel manganese oxides for advanced lithium-ion batteries: toward rechargeable capacity more than 300 mA h g^{-1} . *J. Mater. Chem.* **21**, 10179–10188, <https://doi.org/10.1039/c0jm04325g> (2011).
- Yu, H. & Zhou, H. High-Energy Cathode Materials (Li_2MnO_3 – LiMO_2) for Lithium-Ion Batteries. *J. Phys. Chem. Lett.* **4**, 1268–1280, <https://doi.org/10.1021/jz400032v> (2013).
- Yan, J., Liu, X. & Li, B. Recent progress in Li-rich layered oxides as cathode materials for Li-ion batteries. *RSC Adv* **4**, 63268–63284, <https://doi.org/10.1039/c4ra12454e> (2014).
- Hong, J., Gwon, H., Jung, S. –K., Ku, K. & Kang, K. Review–Lithium-Excess Layered Cathodes for Lithium Rechargeable Batteries. *J. Electrochem. Soc.* **162**, A2447–2467, <https://doi.org/10.1149/2.0071514jes> (2015).
- Zheng, J. *et al.* Li- and Mn-Rich Cathode Materials: Challenges to Commercialization. *Adv. Energy Mater* **7**, 1601284, <https://doi.org/10.1002/aenm.201601284> (2017).
- Erickson, E. M. *et al.* Review–Recent Advances and Remaining Challenges for Lithium Ion Battery Cathodes II. Lithium-Rich, x Li_2MnO_3 (1-x) $\text{LiNi}_x\text{Co}_y\text{Mn}_z\text{O}_2$. *J. Electrochem. Soc.* **164**, A6341–6348, <https://doi.org/10.1149/2.0461701jes> (2017).

10. Nayak, P. K. *et al.* Review on Challenges and Recent Advances in the Electrochemical Performance of High Capacity Li- and Mn-Rich Cathode Materials for Li-Ion Batteries. *Adv. Energy Mater.* **8**, 1702397, <https://doi.org/10.1002/aenm.201702397> (2018).
11. Song, B., Liu, Z., Lai, M. O. & Lu, L. Structural evolution and the capacity fade mechanism upon long-term cycling in Li-rich cathode material. *Phys. Chem. Chem. Phys.* **14**, 12875–12883, <https://doi.org/10.1039/c2cp42068f> (2012).
12. Bettge, M. *et al.* Voltage Fade of Layered Oxides: Its Measurement and Impact on Energy Density. *J. Electrochem. Soc.* **160**, A2046–2055, <https://doi.org/10.1149/2.034311jes> (2013).
13. Wei, Z. *et al.* Correlation between transition metal ion migration and the voltage ranges of electrochemical process for lithium-rich manganese-based material. *J. Power Sources* **281**, 7–10, <https://doi.org/10.1016/j.jpowsour.2015.01.149> (2015).
14. Chen, C. -J. *et al.* The Origin of Capacity Fade in the Li_2MnO_3 LiMO_2 (M = Li, Ni, Co, Mn) Microsphere Positive Electrode: An Operando Neutron Diffraction and Transmission X-ray Microscopy Study. *J. Am. Chem. Soc.* **138**, 8824–8833, <https://doi.org/10.1021/jacs.6b03932> (2016).
15. Barenó, J. *et al.* Long-Range and Local Structure in the Layered Oxide $\text{Li}_{1.2}\text{Co}_{0.4}\text{Mn}_{0.4}\text{O}_2$. *Chem. Mater.* **23**, 2039–2050, <https://doi.org/10.1021/cm200250a> (2011).
16. Boulineau, A. *et al.* Evolutions of $\text{Li}_{1.2}\text{Mn}_{0.6}\text{Ni}_{0.18}\text{Mg}_{0.01}\text{O}_2$ during the Initial Charge/Discharge Cycle Studied by Advanced Electron Microscopy. *Chem. Mater.* **24**, 3558–3566, <https://doi.org/10.1021/cm301140g> (2012).
17. Gu, M. *et al.* Formation of the Spinel Phase in the Layered Composite Cathode Used in Li-Ion Batteries. *ACS Nano* **7**, 760–767, <https://doi.org/10.1021/nn305065u> (2013).
18. Yu, H. *et al.* Direct Atomic-Resolution Observation of Two Phases in the $\text{Li}_{1.2}\text{Mn}_{0.567}\text{Ni}_{0.166}\text{Co}_{0.067}\text{O}_2$ Cathode Material for Lithium-Ion Batteries. *Angew. Chem. Int. Ed.* **52**, 5969–5973, <https://doi.org/10.1002/anie.201301236> (2013).
19. Yu, X. *et al.* Understanding the Rate Capability of High-Energy-Density Li-Rich Layered $\text{Li}_{1.2}\text{Ni}_{0.15}\text{Co}_{0.1}\text{Mn}_{0.55}\text{O}_2$ Cathode Materials. *Adv. Energy Mater.* **4**, 1300950, <https://doi.org/10.1002/aenm.201300950> (2014).
20. Jarvis, K. A., Deng, Z., Allard, L. F., Manthiram, A. & Ferreira, P. J. Atomic Structure of a Lithium-Rich Layered Oxide Material for Lithium-Ion Batteries: Evidence of a Solid Solution. *Chem. Mater.* **23**, 3614–3621, <https://doi.org/10.1021/cm200831c> (2011).
21. Genevois, C. *et al.* Insight into the Atomic Structure of Cycled Lithium-Rich Layered Oxide $\text{Li}_{1.20}\text{Mn}_{0.54}\text{Co}_{0.13}\text{Ni}_{0.13}\text{O}_2$ Using HAADF STEM and Electron Nanodiffraction. *J. Phys. Chem. C* **119**, 75–83, <https://doi.org/10.1021/jp509388j> (2015).
22. Shukla, A. K. *et al.* Unravelling structural ambiguities in lithium- and manganese-rich transition metal oxides. *Nat. Commun.* **6**, 8711, <https://doi.org/10.1038/ncomms9711> (2015).
23. Pan, C., Lee, Y. J., Ammundsen, B. & Grey, C. P. ^6Li MAS NMR Studies of the Local Structure and Electrochemical Properties of Cr-doped Lithium Manganese and Lithium Cobalt Oxide Cathode Materials for Lithium-Ion Batteries. *Chem. Mater.* **14**, 2289–2299, <https://doi.org/10.1021/cm011623u> (2002).
24. Yoon, W. -S., Kim, N., Yang, X. -Q., McBreen, J. & Grey, C. P. ^6Li MAS NMR and *in situ* X-ray studies of lithium nickel manganese oxides. *J. Power Sources* **119**–**121**, 649–653, [https://doi.org/10.1016/S0378-7753\(03\)00195-2](https://doi.org/10.1016/S0378-7753(03)00195-2) (2003).
25. Yoon, W. -S. *et al.* Local Structure and Cation Ordering in O3 Lithium Nickel Manganese Oxides with Stoichiometry $\text{Li}[\text{Ni}_x\text{Mn}_{(2-x)/3}\text{Li}_{(1-2x)/3}]\text{O}_2$. *Electrochem. Solid-State Lett.* **7**, A167–171, <https://doi.org/10.1149/1.1737711> (2004).
26. Lu, Z. & Dahn, J. R. Understanding the Anomalous Capacity of $\text{Li}[\text{Li}[\text{Ni}_{(1/3-2x/3)}\text{Mn}_{(2/3-x/3)}]\text{O}_2$ Cells Using *In Situ* X-Ray Diffraction and Electrochemical Studies. *J. Electrochem. Soc.* **149**, A815–822, <https://doi.org/10.1149/1.1480014> (2002).
27. Simonin, L. *et al.* *In situ* investigations of a Li-rich Mn–Ni layered oxide for Li-ion batteries. *J. Mater. Chem.* **22**, 11316–11322, <https://doi.org/10.1039/c2jm31205k> (2012).
28. Mohanty, D. *et al.* Structural transformation of a lithium-rich $\text{Li}_{1.2}\text{Co}_{0.1}\text{Mn}_{0.55}\text{Ni}_{0.15}\text{O}_2$ cathode during high voltage cycling resolved by *in situ* X-ray diffraction. *J. Power Sources* **229**, 239–248, <https://doi.org/10.1016/j.jpowsour.2012.11.144> (2013).
29. Li, J., Shunmugasundaram, R., Doig, R. & Dahn, J. R. *In Situ* X-ray Diffraction Study of Layered Li–Ni–Mn–Co Oxides: Effect of Particle Size and Structural Stability of Core–Shell Materials. *Chem. Mater.* **28**, 162–171, <https://doi.org/10.1021/acs.chemmater.5b03500> (2016).
30. Ito, A. *et al.* *In situ* X-ray absorption spectroscopic study of Li-rich layered cathode material $\text{Li}[\text{Ni}_{0.17}\text{Li}_{0.2}\text{Co}_{0.07}\text{Mn}_{0.56}]\text{O}_2$. *J. Power Sources* **196**, 6828–6834, <https://doi.org/10.1016/j.jpowsour.2010.09.105> (2011).
31. Koga, H. *et al.* Operando X-ray Absorption Study of the Redox Processes Involved upon Cycling of the Li-Rich Layered Oxide $\text{Li}_{1.2}\text{Mn}_{0.54}\text{Co}_{0.13}\text{Ni}_{0.13}\text{O}_2$ in Li Ion Batteries. *J. Phys. Chem. C* **118**, 5700–5709, <https://doi.org/10.1021/jp412197z> (2014).
32. Oishi, M. *et al.* Charge compensation mechanisms in $\text{Li}_{1.16}\text{Ni}_{0.15}\text{Co}_{0.19}\text{Mn}_{0.50}\text{O}_2$ positive electrode material for Li-ion batteries analyzed by a combination of hard and soft X-ray absorption near edge structure. *J. Power Sources* **222**, 45–51, <https://doi.org/10.1016/j.jpowsour.2012.08.023> (2013).
33. Oishi, M. *et al.* Direct observation of reversible charge compensation by oxygen ion in Li-rich manganese layered oxide positive electrode material, $\text{Li}_{0.16}\text{Ni}_{0.15}\text{Co}_{0.19}\text{Mn}_{0.50}\text{O}_2$. *J. Power Sources* **276**, 89–94, <https://doi.org/10.1016/j.jpowsour.2014.11.104> (2015).
34. Luo, K. *et al.* Charge-compensation in 3d-transition-metal-oxide intercalation cathodes through the generation of localized electron holes on oxygen. *Nat. Chem.* **8**, 684–691, <https://doi.org/10.1038/nchem.2471> (2016).
35. Luo, K. *et al.* Anion Redox Chemistry in the Cobalt Free 3d Transition Metal Oxide Intercalation Electrode $\text{Li}[\text{Li}_{0.2}\text{Ni}_{0.2}\text{Mn}_{0.6}]\text{O}_2$. *J. Am. Chem. Soc.* **138**, 11211–11218, <https://doi.org/10.1021/jacs.6b05111> (2016).
36. Gent, W. E. *et al.* Coupling between oxygen redox and cation migration explains unusual electrochemistry in lithium-rich layered oxides. *Nat. Commun.* **8**, 2091, <https://doi.org/10.1038/s41467-017-02041-x> (2017).
37. Xu, J. *et al.* Elucidating anionic oxygen activity in lithium-rich layered oxides. *Nat. Commun.* **9**, 947, <https://doi.org/10.1038/s41467-018-03403-9> (2018).
38. Jiang, M., Key, B., Meng, Y. S. & Grey, C. P. Electrochemical and Structural Study of the Layered, “Li-Excess” Lithium-Ion Battery Electrode Material $\text{Li}[\text{Li}_{1/9}\text{Ni}_{1/3}\text{Mn}_{5/9}]\text{O}_2$. *Chem. Mater.* **21**, 2733–2745, <https://doi.org/10.1021/cm900279u> (2009).
39. Buzlukov, A. *et al.* Li-Rich Mn/Ni Layered Oxide as Electrode Material for Lithium Batteries: A ^7Li MAS NMR Study Revealing Segregation into (Nanoscale) Domains with Highly Different Electrochemical Behaviors. *J. Phys. Chem. C* **120**, 19049–19063, <https://doi.org/10.1021/acs.jpcc.6b07532> (2016).
40. Hung, I., Zhou, L., Pourpoint, F., Grey, C. P. & Gan, Z. Isotropic High Field NMR Spectra of Li-Ion Battery Materials with Anisotropy > 1 MHz. *J. Am. Chem. Soc.* **134**, 1898–1901, <https://doi.org/10.1021/ja209600m> (2012).
41. Li, X. *et al.* Lithiation and Delithiation Dynamics of Different Li Sites in Li-Rich Battery Cathodes Studied by Operando Nuclear Magnetic Resonance. *Chem. Mater.* **29**, 8282–8291, <https://doi.org/10.1021/acs.chemmater.7b02589> (2017).
42. Matsunaga, T. *et al.* Structural Understanding of Superior Battery Properties of Partially Ni-Doped Li_2MnO_3 as Cathode Material. *J. Phys. Chem. Lett.* **7**, 2063–2067, <https://doi.org/10.1021/acs.jpcclett.6b00587> (2016).
43. Shimoda, K. *et al.* Oxidation behaviour of lattice oxygen in Li-rich manganese-based layered oxide studied by hard X-ray photoelectron spectroscopy. *J. Mater. Chem. A* **4**, 5909–5916, <https://doi.org/10.1039/c6ta01152g> (2016).
44. Koga, H. *et al.* Different oxygen redox participation for bulk and surface: A possible global explanation for the cycling mechanism of $\text{Li}_{1.20}\text{Mn}_{0.54}\text{Co}_{0.13}\text{Ni}_{0.13}\text{O}_2$. *J. Power Sources* **236**, 250–258, <https://doi.org/10.1016/j.jpowsour.2013.02.075> (2013).
45. Thackeray, M. M., de Kock, A. & David, W. I. F. Synthesis and structural characterization of defect spinels in the lithium-manganese-oxide system. *Mater. Res. Bull.* **28**, 1041–1049, [https://doi.org/10.1016/0025-5408\(93\)90142-z](https://doi.org/10.1016/0025-5408(93)90142-z) (1993).
46. Amalraj, F. *et al.* Study of the Lithium-Rich Integrated Compound $x\text{Li}_2\text{MnO}_3 \cdot (1-x)\text{LiMO}_2$ (x around 0.5; M = Mn, Ni, Co; 2:2:1) and Its Electrochemical Activity as Positive Electrode in Lithium Cells. *J. Electrochem. Soc.* **160**, A324–337, <https://doi.org/10.1149/2.070302jes> (2013).

47. Ito, A. *et al.* Direct observation of the partial formation of a framework structure for Li-rich layered cathode material $\text{Li}[\text{Ni}_{0.17}\text{Li}_{0.02}\text{Co}_{0.07}\text{Mn}_{0.56}]\text{O}_2$ upon the first charge and discharge. *J. Power Sources* **196**, 4785–4790, <https://doi.org/10.1016/j.jpowsour.2010.12.079> (2011).
48. Shen, C. *–H. et al.* New insight into structural transformation in Li-rich layered oxide during the initial charging. *J. Mater. Chem. A* **3**, 12220–12229, <https://doi.org/10.1039/c5ta01849h> (2015).
49. Komatsu, H. *et al.* Site-Selective Analysis of Nickel-Substituted Li-Rich Layered Material: Migration and Role of Transition Metal at Charging and Discharging. *J. Phys. Chem. C* **122**, 20099–20107, <https://doi.org/10.1021/acs.jpcc.8b05539> (2018).
50. Qian, D., Xu, B., Chi, M. & Meng, Y. S. Uncovering the roles of oxygen vacancies in cation migration in lithium excess layered oxides. *Phys. Chem. Chem. Phys.* **16**, 14665–14668, <https://doi.org/10.1039/c4cp01799d> (2014).
51. Muhammad, S. *et al.* Evidence of reversible oxygen participation in anomalously high capacity Li- and Mn-rich cathodes for Li-ion batteries. *Nano Energy* **21**, 172–184, <https://doi.org/10.1016/j.nanoen.2015.12.027> (2016).
52. Montoro, L. A., Abbate, M., Almeida, E. C. & Rosolen, J. M. Electronic structure of the transition metal ions in LiCoO_2 , LiNiO_2 and $\text{LiCo}_{0.5}\text{Ni}_{0.5}\text{O}_2$. *Chem. Phys. Lett.* **309**, 14–18, [https://doi.org/10.1016/S0009-2614\(99\)00650-8](https://doi.org/10.1016/S0009-2614(99)00650-8) (1999).
53. Xu, J. *et al.* Understanding the Degradation Mechanism of Lithium Nickel Oxide Cathodes for Li-Ion Batteries. *ACS Appl. Mater. Interfaces* **8**, 31677–31683, <https://doi.org/10.1021/acsami.6b11111> (2016).
54. Hy, S. *et al.* Understanding the Role of Ni in Stabilizing the Lithium-Rich High-Capacity Cathode Material $\text{Li}[\text{Ni}_x\text{Li}_{(1/3-2x/3)}\text{Mn}_{(2/3-x/3)}]\text{O}_2$ ($0 \leq x \leq 0.5$). *Chem. Mater.* **26**, 6919–6927, <https://doi.org/10.1021/cm501664y> (2014).
55. Oishi, M. *et al.* Direct observation of reversible oxygen anion redox reaction in Li-rich manganese oxide, Li_2MnO_3 , studied by soft X-ray absorption spectroscopy. *J. Mater. Chem. A* **4**, 9293–9302, <https://doi.org/10.1039/c6ta00174b> (2016).
56. Shimoda, K. *et al.* Direct observation of layered-to-spinel phase transformation in Li_2MnO_3 and the spinel structure stabilised after the activation process. *J. Mater. Chem. A* **5**, 6695–6707, <https://doi.org/10.1039/c6ta11151c> (2017).
57. Uchimoto, Y., Sawada, H. & Yao, T. Changes in electronic structure by Li ion deintercalation in LiNiO_2 from nickel L-edge and O K-edge XANES. *J. Power Sources* **97–98**, 326–327, [https://doi.org/10.1016/S0378-7753\(01\)00624-3](https://doi.org/10.1016/S0378-7753(01)00624-3) (2001).
58. Uchimoto, Y., Sawada, H. & Yao, T. Changes in electronic structure by Li ion deintercalation in LiCoO_2 from cobalt L-edge and oxygen K-edge XANES. *J. Synchrotron Rad* **8**, 872–873, <https://doi.org/10.1107/S0909049500020938> (2001).
59. Yoon, W. *–S. et al.* Soft X-Ray Absorption Spectroscopic Study of a $\text{LiNi}_{0.5}\text{Mn}_{0.5}\text{O}_2$ Cathode during Charge. *J. Electrochem. Soc.* **151**, A246–251, <https://doi.org/10.1149/1.1637896> (2004).
60. Yoon, W. *–S. et al.* Combined NMR and XAS Study on Local Environments and Electronic Structures of Electrochemically Li-Ion Deintercalated Li Co Ni Mn O Electrode System. *Electrochem. Solid-State Lett* **7**, A53–55, <https://doi.org/10.1149/1.1643592> (2004).
61. Kim, M. G., Shin, H. J., Kim, J. *–H.*, Park, S. *–H.*, Sun, Y. & XAS Investigation, K. of Inhomogeneous Metal-Oxygen Bond Covalency in Bulk and Surface for Charge Compensation in Li-Ion Battery Cathode $\text{Li}[\text{Ni}_{1-x}\text{Co}_{1/3}\text{Mn}_{1/3}]\text{O}_2$ Material. *J. Electrochem. Soc.* **152**, A1320–1328, <https://doi.org/10.1149/1.1926647> (2005).
62. Qiao, R., Chuang, Y. *–D.*, Yan, S. & Yang, W. Soft X-Ray Irradiation Effects of Li_2O_2 , Li_2CO_3 and Li_2O Revealed by Absorption Spectroscopy. *PLoS ONE* **7**, e49182, <https://doi.org/10.1371/journal.pone.0049182> (2012).
63. Li, X. *et al.* Direct Visualization of the Reversible O^{2-}/O^- Redox Process in Li-Rich Cathode Materials. *Adv. Mater.* **30**, 1705197, <https://doi.org/10.1002/adma.201705197> (2018).
64. Dogan, F. *et al.* Re-entrant Lithium Local Environments and Defect Driven Electrochemistry of Li- and Mn-Rich Li-Ion Battery Cathodes. *J. Am. Chem. Soc.* **137**, 2328–2335, <https://doi.org/10.1021/ja511299y> (2015).
65. Ménétrier, M., Saadoune, I., Levasseur, S. & Delmas, C. The insulator–metal transition upon lithium deintercalation from LiCoO_2 : electronic properties and Li NMR study. *J. Mater. Chem.* **9**, 1135–1140, <https://doi.org/10.1039/A900016j> (1999).
66. Shimoda, K. *et al.* Delithiation/Lithiation Behavior of $\text{LiNi}_{0.5}\text{Mn}_{1.5}\text{O}_4$ Studied by *In Situ* and *Ex Situ* ^6Li NMR Spectroscopy. *J. Phys. Chem. C* **119**, 13472–13480, <https://doi.org/10.1021/acs.jpcc.5b03273> (2015).
67. Kikkawa, J. *et al.* Real-Space Observation of Li Extraction/Insertion in $\text{Li}_{1.2}\text{Mn}_{0.4}\text{Fe}_{0.4}\text{O}_2$ Positive Electrode Material for Li-Ion Batteries. *Electrochem. Solid-State Lett.* **11**, A183–186, <https://doi.org/10.1149/1.2968956> (2008).
68. Liu, H. *et al.* Unraveling the Rapid Performance Decay of Layered High-Energy Cathodes: From Nanoscale Degradation to Drastic Bulk Evolution. *ACS Nano* **12**, 2708–2718, <https://doi.org/10.1021/acsnano.7b08945> (2018).
69. Petricek, V., Dusek, M. & Palatinus, L. Crystallographic Computing System JANA2006: General features. *Z. Kristallogr* **229**, 345–352, <https://doi.org/10.1515/zkri-2014-1737> (2014).
70. Achkar, A. J. *et al.* Bulk sensitive x-ray absorption spectroscopy free of self-absorption effects. *Phys. Rev. B* **83**, 081106, <https://doi.org/10.1103/PhysRevB.83.081106> (2011).
71. Yoon, W. *–S. et al.* Investigation of the Charge Compensation Mechanism on the Electrochemically Li-Ion Deintercalated $\text{Li}_{1-x}\text{Co}_{1/3}\text{Ni}_{1/3}\text{Mn}_{1/3}\text{O}_2$ Electrode System by Combination of Soft and Hard X-ray Absorption Spectroscopy. *J. Am. Chem. Soc.* **127**, 17479–17487, <https://doi.org/10.1021/ja0530568> (2005).

Acknowledgements

This work was supported by the Research and Development Initiative for Scientific Innovation of New Generation Batteries 2 (RISING2) project, JPNP16001, from the New Energy and Industrial Technology Development Organization (NEDO), Japan. The authors would like to thank Mr. Takashi Moroishi for his support during sample preparation and electrochemical measurements. The authors are deeply grateful to Ms. Hiromi Sekiguchi and Dr. Nobuto Nakanishi of Thermo Fisher Scientific for their support regarding the HAADF-STEM measurements. The authors are also grateful to Prof. Iwao Watanabe for his fruitful discussions regarding the soft XAS measurements. The synchrotron-radiation XRD measurements were performed with the approval of the Japan Synchrotron Radiation Research Institute (JASRI, Proposal No. 2016B7611).

Author contributions

The manuscript was written through contributions of all authors; K.S. and T.M. prepared samples. K.S. and T.M. performed synchrotron-radiation XRD measurements and Rietveld refinements. K.S., K.Yam, and T.O. performed soft XAS measurements and contributed to discussions of the results. K.S., K.Yaz, and M.M. performed NMR measurements and contributed to discussions of the results. E.M., Z.O. and T.A. supervised the project. K.S. wrote the manuscript with contributions from all authors.

Competing interests

The authors declare no competing interests.

Additional information

Supplementary information is available for this paper at <https://doi.org/10.1038/s41598-020-66411-0>.

Correspondence and requests for materials should be addressed to K.S.

Reprints and permissions information is available at www.nature.com/reprints.

Publisher's note Springer Nature remains neutral with regard to jurisdictional claims in published maps and institutional affiliations.



Open Access This article is licensed under a Creative Commons Attribution 4.0 International License, which permits use, sharing, adaptation, distribution and reproduction in any medium or format, as long as you give appropriate credit to the original author(s) and the source, provide a link to the Creative Commons license, and indicate if changes were made. The images or other third party material in this article are included in the article's Creative Commons license, unless indicated otherwise in a credit line to the material. If material is not included in the article's Creative Commons license and your intended use is not permitted by statutory regulation or exceeds the permitted use, you will need to obtain permission directly from the copyright holder. To view a copy of this license, visit <http://creativecommons.org/licenses/by/4.0/>.

© The Author(s) 2020